Solar-Terrestrial Physics. 2019. Vol. 5. Iss. 4. P. 27–33. DOI: 10.12737/stp-54201904. © 2019
A.Yu. Fedotova, A.T. Altyntsev, A.A. Kochanov, S.V. Lesovoi, N.S. Meshalkina. Published by INFRA-M Academic Publishing House
Original Russian version: A.Yu. Fedotova, A.T. Altyntsev, A.A. Kochanov, S.V. Lesovoi, N.S. Meshalkina, published in Solnechno-zemnaya fizika. 2019. Vol. 5. Iss. 4. P. 34–41. DOI: 10.12737/szf-54201904. © 2019 INFRA-M Academic Publishing House (Nauchno-Izdatelskii Tsentr INFRA-M)

CALIBRATION OF SIBERIAN RADIOHELIOGRAPH IMAGES

A.Yu. Fedotova
Institute of Solar-Terrestrial Physics SB RAS, Irkutsk, Russia, fedotovanastya@iszf.irk.ru

A.T. Altyntsev
Institute of Solar-Terrestrial Physics SB RAS, Irkutsk, Russia, altyntsev@iszf.irk.ru

A.A. Kochanov
Institute of Solar-Terrestrial Physics SB RAS, Irkutsk, Russia, kochanov@iszf.irk.ru

S.V. Lesovoi
Institute of Solar-Terrestrial Physics SB RAS, Irkutsk, Russia, svlesovoi@gmail.com

N.S. Meshalkina
Institute of Solar-Terrestrial Physics SB RAS, Irkutsk, Russia, nata@iszf.irk.ru

Abstract. We discuss the method for automatic calibration of solar radio images derived from the first stage of the multiwave Siberian Radioheliograph (SRH-48). SRH is a 48-element T-shaped radiointerferometer in the 4–8 GHz frequency range. Since the end of 2017, the number of frequencies has been increased to 32. The method is implemented in Python programming language. We give examples of calibration for SRH instrument values in brightness temperature of the quiet and active Sun at several frequencies for four eruptive events: June 19, 2017, July 25, 2016, April 24, 2017, and April 19, 2017. In conclusion, we present spectra for three events, as well as brightness temperature estimates by flux, angular size of filaments, and emission measure.

Keywords: radioheliograph, Sun, image calibration, eruptive events, spectrum.

INTRODUCTION

Effective use of observational data from multiwave radioheliographs to diagnose parameters of microwave sources involves solving such methodological problems as radio imaging, conversion of instrumental radio brightness into brightness temperatures, cleaning of images from the contribution of side lobes.

Sensitivity of radioheliographs is insufficient to observe calibrated stellar sources and requires the implementation of methods that differ from methods for calibrating stellar interferometers. We have used observational experience of the radioheliographs that monitor solar activity in the microwave range: Siberian Solar Radio Telescope (SSRT) [http://ru.iszf.irk.ru; Grechnev et al., 2003; Kochanov et al., 2013] and Nobeyama radioheliograph (NoRH) [https://solar.nro.nao.ac.jp/norh/html; Nakajima et al., 1995].

The calibration method is based on the comparison between instrumental values of radio brightness of the sky, i.e. the frame part outside the solar disk, and regions of the quiet Sun whose difference corresponds to the brightness temperature of the quiet Sun. By the quiet Sun is meant areas without active regions, other local sources, and eruptions on the solar disk. As reference values of brightness temperatures of the quiet Sun we have utilized the values obtained in [Zirin et al., 1991; Borovik, 1994]. In these papers, telescopes were calibrated using lunar observations, and solar emission was measured in a frequency range 1.4–18 GHz during solar minimum. Objectives of this paper are: 1) to describe step by step the conversion of instrumental radio brightness values into brightness temperature values using SRH data obtained during solar minimum; 2) to test the performance of the method for active and quiet Sun.

1. SIBERIAN RADIOHELIOGRAPH. MAIN CHARACTERISTICS

The first stage of SRH is a new-generation multiwavelength radio interferometer providing solar disk images at selected frequencies in the range 4–8 GHz. Observations are made with a 48-antenna T-shaped array and receiving system allowing aperture synthesis [Lesovoi et al., 2017]. Receiving frequencies are changed by selecting from a given list of frequencies.

From late July 2016 to 2017, observations were carried out at five frequencies (4.5, 5.2, 6.0, 6.8, and 7.5 GHz), and since the end of 2017 the number of frequencies has been increased to 32. The spatial resolution of SRH is ~1.2–2 arcmin in the 4–8 GHz frequency range. Routine observations are made throughout daylight hours: in summer from 00:00 to 10:00 UT, in winter from 02:00 to 08:00 UT. Observations with the first stage of SRH are currently used for testing systems and data analysis algorithms of the radioheliograph developed at the ISTP SB RAS Radioastrophysical Observatory for the frequency range 3–24 GHz; its construction is scheduled for completion in 2020–2021.

The real-time monitoring of the state of the instrument and microwave solar emission variations is provided using the so-called correlation curves [badary.iszf.irk.ru]. The calculation algorithm and characteristics of SRH correlation curves are presented in [Lesovoi, Kobets, 2017]. Variations in the correlation curves are roughly proportional to time variations in the total solar emission.

1.1. Calibration method

The calibration method is described by the example of the quiet Sun for March 26, 2018 when there were no

bright sources on the solar disk and images did not need "cleaning" from side-lobe contribution. Input data is records of pairwise correlations of SRH antenna signals in FITS format at predetermined frequencies in the range 4–8 GHz. To source files we apply the srh-data library [https://git.iszf.irk.ru/kochanov/srh48–api] written in Python programming language, which allows us to form raw radio images of the solar disk and file them.

In the case of solar observations at five frequencies, one file with raw data comprises 100 images with primary values of solar radio brightness: 20 frames for each frequency with left and right circular polarizations (RCP, LCP).

The signal recording cycles at five frequencies in two polarizations were repeated every 5–6 s. There are date and time of observation, object, telescope, observatory coordinates, number of channels and frequencies in the file header. The solar image frame size for SRH is the same for each frequency and is 512×512 pixels, the pixel weight is 4.911 arcsec. The solar diameter for all frequencies is ~192 pixels.

Note that in some cases the quality of the calibration is affected by a possible shift of the solar disk relative to the frame center and appearance of distortions in sky regions associated with the response to the Sun in the adjacent orders of the radioheliograph. The distortions may be significant for the observation time away from the local noon (05:00 UT).

Figure 1 gives examples of calibrated images in palettes of brightness temperatures (right scale) for frequencies of 4.25 and 5.2 GHz at 03:59 UT on March 26, 2018. Brightnesses of the solar disk and sky differ significantly.

The calibration procedure consists of two stages — full-frame pre-calibration and mask calibration. In Figure 2, the red color marks histograms of per-pixel radio brightness of a full frame. There are two groups of pixels differing in brightness. The first group of pixels for which instrumental brightness values (dimensionless value shown by the scale at the top) vary around zero corresponds to the sky. The second group of pixels refers to the solar disk, and the shape of this part of the histogram can be approximated by a Gaussian curve with the mean instrumental brightness μ and the standard deviation σ.

After identifying these Gaussian distribution parameters in the frame, we excluded regions whose brightness was outside μ+2.5σ (dark areas on the solar disk in Figure 1) from further calibration. The next stage of the calibration is to separate areas of the sky and quiet Sun. After centering the solar disk to the frame, we superimposed circle masks with diameter by 20 % larger and 20 % smaller than the disk of the quiet Sun.

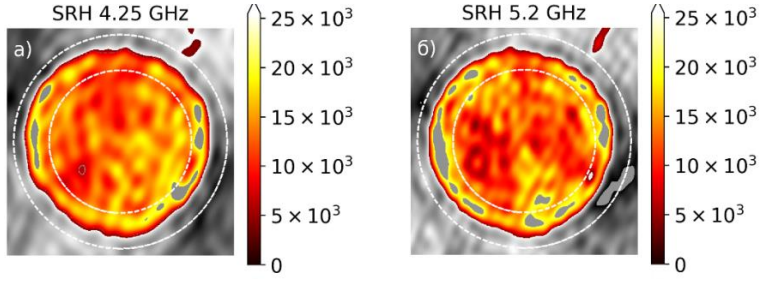

Figure 1. Calibrated images in brightness temperature values (K) with masks (white contours) superimposed on areas of the sky and quiet Sun at frequencies of 4.25 GHz (*a*) and 5.2 GHz (*b*) at 03:59 UT on March 26, 2018

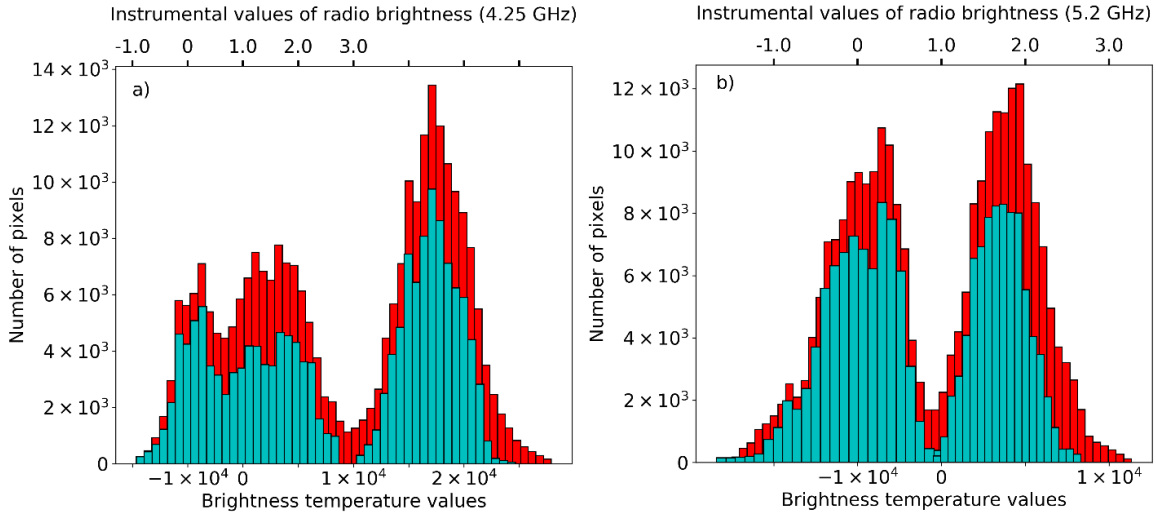

Figure 2. Calibrated histograms as derived from SRH data at 4.25 GHz (*a*) and 5.2 GHz (*b*) (red) at 03:59 UT on March 26, 2018. The blue color indicates histograms of masks for areas of the sky and quiet Sun. Along the X-axis are brightness temperatures (K); along the Y-axis is the number of pixels

Thus, we used two masks: for the area of the sky outside a circle 238 pixels in radius and the area of the quiet Sun inside a circle 164 pixels in radius (Figure 1). Bounding the areas by the masks eliminates the contribution of limb brightenings, prominences, and other near-limb structures. Histograms for the corrected areas of images are shown in Figure 2 in blue. In this case, shapes of the histograms for the full frame and areas of the sky and Sun are similar. Since the shape of the histogram for the sky is still significantly different from the Gaussian distribution, as an instrumental brightness of the sky and Sun we take centroids of the histograms.

Figure 3 shows probability distributions of instrumental values of per-pixel radio brightness at 03:59 UT on March 26, 2018 for areas of the sky (*a*, *c*) and the Sun (*b*, *d*) as derived from SRH data at 4.25 GHz (*a*, *b*) and 5.2 GHz (*c*, *d*). Instrumental values of centroids of the sky $sky_{lev}(f)$ and Sun $Sun_{lev}(f)$ correspond to probability levels of 0.5. Differences between the observed positions of the centroids of the model Gaussian dependences (dashed lines) at the 0.5 level are insignificant both for the sky and for the Sun. Calibration implies that each image pixel is assigned a brightness temperature value

$$C(f)=\left(\frac{Image-sky_{lev}(f)}{Sun_{lev}(f)-sky_{lev}(f)}\right)\times T_b(f), \qquad (1)$$

where $T_b(f)$ is the brightness temperature of the quiet Sun, which is defined for each frequency taken from [Zirin et al., 1991; Borovik, 1994] (Table 1).

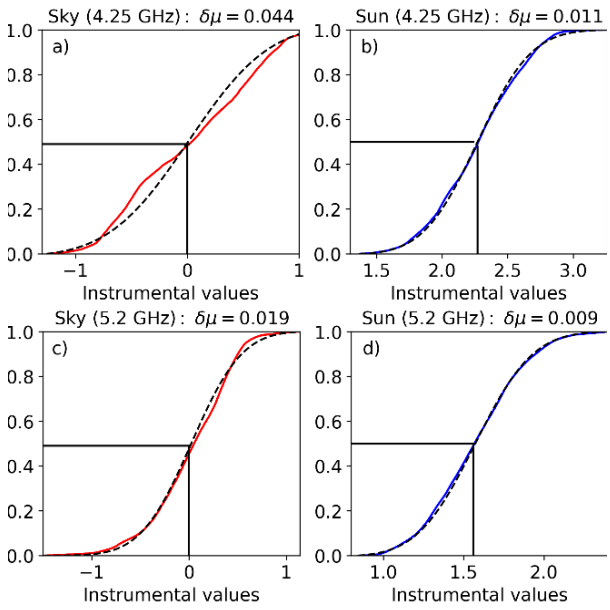

Figure 3. Normalized function of distribution of instrumental values of per-pixel radio brightness (dimensionless value) for the sky (red line) and for the quiet Sun (blue line) at 4.25 GHz (*a*, *b*) and 5.2 GHz (*c*, *d*) at 03:59 UT on March 26, 2018. The black dashed line is the normal distribution function corresponding to the approximation of the histograms of masks in Figure 2 by a Gaussian curve. The δμ value characterizes the deviation of the centroid μ from the approximating distribution

The results of calculations of mean instrumental brightness values μ throughout the daylight hours on March 26, 2018 and May 01, 2017 at a frequency of 5.2 GHz are presented in Figure 4. On the first day, no active processes in the solar atmosphere were recorded, and on May 01, 2017 there was a plasma jet in the north-east of the solar limb from 04:00 to 04:50 UT.

The SDO/AIA orbital observatory recorded the jet at wavelengths of 171, 304, 211, and 304 Å [http://suntoday.lmsal.com/suntoday].

The calibration error was estimated from μ and σ variations for a number of sequential frames according to the expression:

$$\Delta x=\left(\sum\frac{\left(x_i-\langle x\rangle\right)^2}{n(n-1)}\right), \qquad (2)$$

where x_i is the numerical result of one measurement, x is μ or σ depending on a specific case, n is the number of measurements.

Table 2 displays corresponding values for 02:59 UT on March 26, 2018 for n=10. In Figure 4, the errors are plotted as bars.

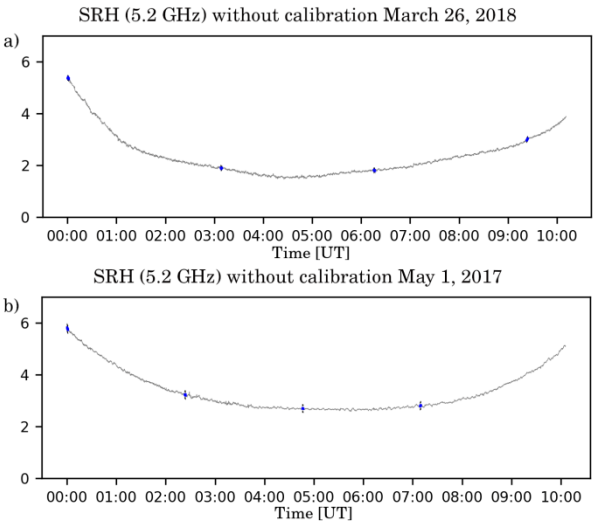

Figure 4. Results of calculations of μ (gray curve) in instrumental values of per-pixel radio brightness before calibration during solar minimum at 5.2 GHz for the whole day of observations from 00:00 to 10:00 UT on March 26, 2018 (*a*). Similar dependences at 5.2 GHz for May 01, 2017 (*b*). Values of the standard deviation σ derived from the statistical analysis of ten sequential frames (bars on μ curves)

Table 1

Brightness temperatures of the quiet Sun in the 4–8 GHz frequency range

Frequency, GHz	Brightness temperature, K
4.5	18 700±300
5.2	17 100±300
6.0	15 400±300
6.8	14 300±300
7.5	13 500±300

Figure 4, *a* shows the μ values for March 26, 2018 calculated for the sky and Sun at 5.2 GHz. The μ value for the area of the sky differs slightly from zero and is –0.028 in per-pixel radio brightness units. The μ plot for the quiet Sun has the form of daily variation with minimum values around the local noon. The error in measuring solar disk shift in the frame, which is determined by Formula (2), is given for four moments. In this case, the standard deviation σ does not exceed 0.034 for the sky and 0.021 for the Sun. The other two frequencies (4.34 and 4.65 GHz) are not displayed in the Figure because they have a similar relationship. Figure 4, *b* shows similar results for May 01, 2017 at 5.2 GHz. For the area of the sky, μ is –0.033 in instrumental units of per-pixel radio brightness.

In this case, the errors do not exceed 0.022 for the Sun and 0.06 for the sky.

Table 2

Results of calculations of calibration errors at 4.34, 4.65, and 5.2 GHz for 02:59 UT of March 26, 2018. Values are given in instrumental units of per-pixel radio brightness after zero shift

Frequency, GHz	The Sun: μ±σ
4.34	1.934±0.015
4.65	1.874±0.005
5.2	1.573±0.014

1.2. June 19, 2017 spray

As an example of the use of the calibrations let us examine the June 19, 2017 ejection that occurred in the northwest of the solar limb. It was recorded by SDO/AIA in extreme ultraviolet channels of 171, 193, 304, 211, and 335 Å in active region AR 12664. SRH observed this spray at frequencies of 4.2 and 5.2 GHz from 04:20 UT.

Figure 5 presents a sequence of frames showing the evolution of the spray from 04:24 to 05:12 UT according to data from SRH at frequencies 4.2 GHz (*a*) and 5.2 GHz (*b*), NoRH at a frequency of 17 GHz (*c*), and SDO at a wavelength of 304 Å (*d*). In view of the differences in spatial resolution, there is good agreement in the position and heights of the ascending spray in the images in various emission ranges. The emergence of the spray above the limb can be seen at~ 04:30 UT, and at 04:40 UT there is a feature in the form of a jet rising to 170 Mm. We superimposed circular masks 192 pixels in diameter on the SRH and NoRH images, which shadow the solar disk. The palettes in use correspond to brightness temperatures for the radioheliographs (SRH, NoRH), for SDO brightness values are given in relative units. White contours mark antenna array patterns for SRH at 4.2 GHz (91″×95′), 5.2 GHz (113″×130″), and NoRH at 17 GHz (12″×12″).

Figure 6 presents light curves of spray emission brightness maxima between 04:00 and 05:30 UT, measured in the white squares in Figure 5, at frequencies of SRH 5.2 GHz (*a*) and NoRH 17 GHz (*b*). The third panel shows the SDO signal value at a wavelength of 304 Å (*c*). Panel *d* presents brightness temperatures as derived from GOES-15 data for two channels of soft and hard X-rays.

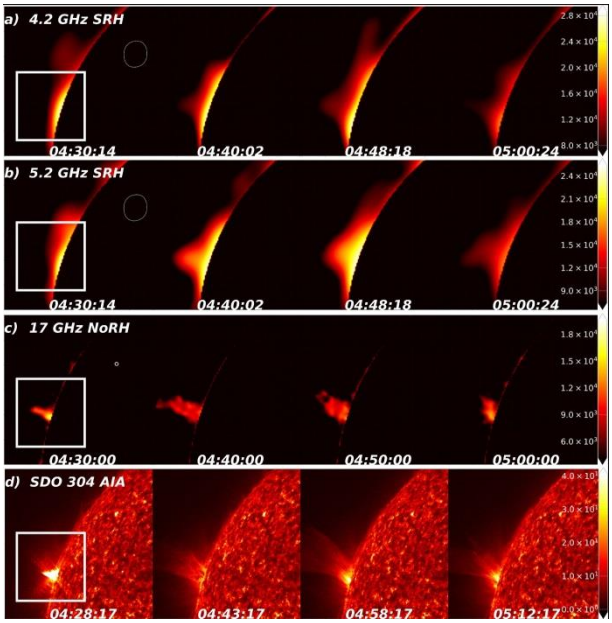

Figure 5. June 19, 2017. A sequence of images of a spray (fan-shaped ejection) when appeared above the limb obtained by SRH at 4.2 and 5.2 GHz (*a*, *b*), NoRH at 17 GHz (*c*), and SDO at 304 Å (*d*). On the right on bars are brightness temperatures. Frame size is 600″×600″. White squares mark the 70″×70″ mask

The brightness temperatures measured with SRH are three times higher than the maximum brightness at 17 GHz and the temperature of the quiet Sun. The real brightness temperatures obtained with SRH may be significantly higher if the size of a source is smaller than the antenna beamwidth. According to the data posted on the website [http://suntoday.lmsal.com/suntoday] at 04:29 UT, GOES recorded a B3.0 flare located a little farther from the northeast of the solar limb (~N17). The SRH light curves are consistent with the time profile of the NoRH brightness temperature, the ratio of the response amplitudes during a flare may be significantly affected by the difference between antenna beam widths of SRH and NoRH: the SRH beam pattern is nine times wider than that of NoRH.

1.3. Discussion

As follows from the above results, spectral measurements are significantly affected by the difference in spatial resolution. This fact should be considered for images taken at different SRH frequencies. Below are spectral estimates for three structures observed on: 1) July 25, 2016; 2) April 24, 2017; 3) April 19, 2017.

The first structure – a system of loops above the east limb –occurred on July 25, 2016 (Figure 7). The radioheliographs observed an extended local source with a bright region in its center. SDO observed the loop system during daylight hours of SRH at seven wavelengths (171, 193, 304, 211, 131, 335, 094 Å), but the bright region detected in the microwave range was not seen in EUV. Later, outside the daylight hours for SRH, this structure produced a filament. Since the size of the bright area of the source according to its image at 17 GHz is much smaller than SRH beam patterns, spectra were calculated in above-the-limb microwave emission fluxes within the frames presented in Figure 7.

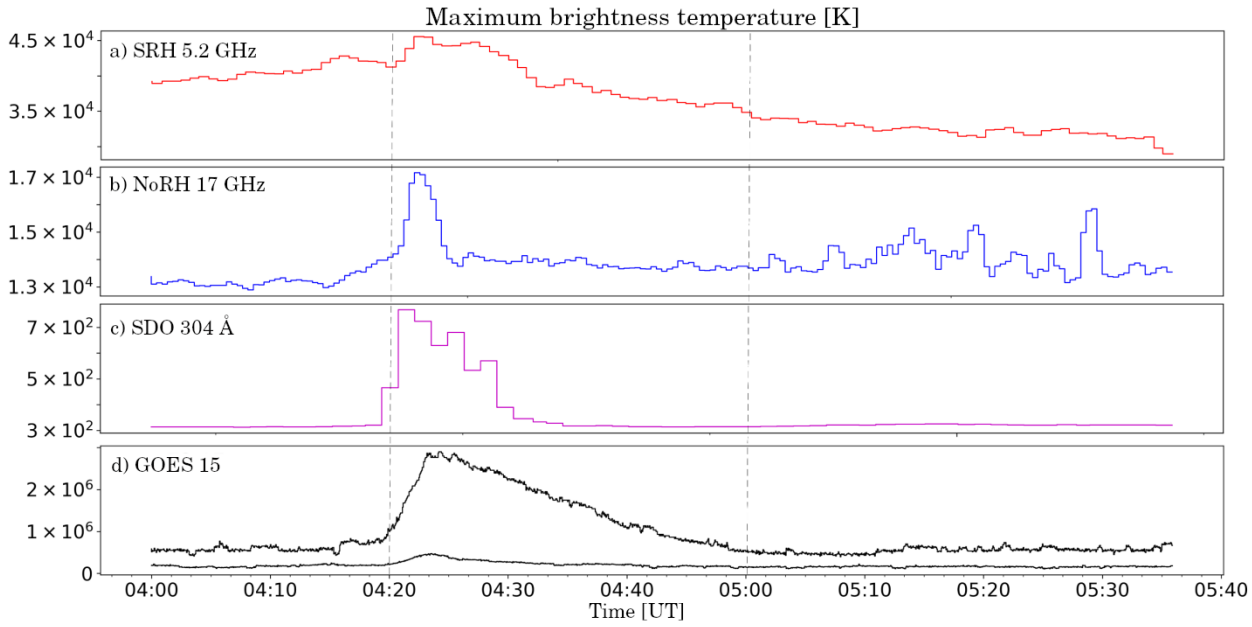

Figure 6. Solar activity variation from 04:00 to 05:30 UT on June 19, 2017 as derived from data from SRH at 5.2 GHz (*a)* and NoRH at 17 GHz (*b*); SDO signal value at 304 Å (*c*); brightness temperatures derived from GOES-15 data in soft and hard X-ray channels (*d*).Vertical dashed lines indicate the time interval 04:20–05:00 UT, during which the evolution of the spray was observed

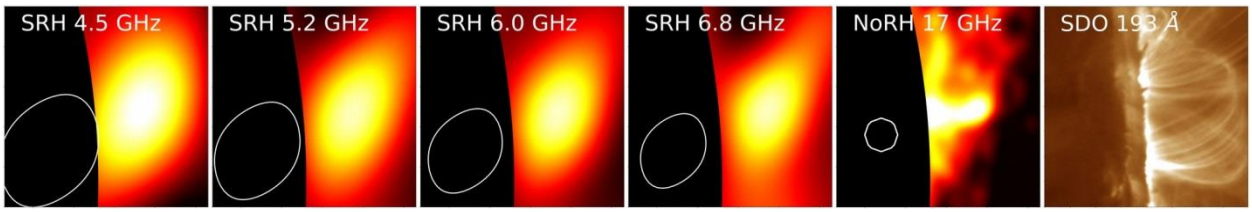

Figure 7. System of hot loops observed in the east of the solar limb at 03:00 UT on July 25, 2016. Images are constructed using data from (left to right): SRH in the frequency range 4.5–6.8 GHz (first four, the white line shows the antenna pattern), NoRH at a frequency of 17 GHz, and SDO at a wavelength of 193 Å. Frame size is 400″×400″

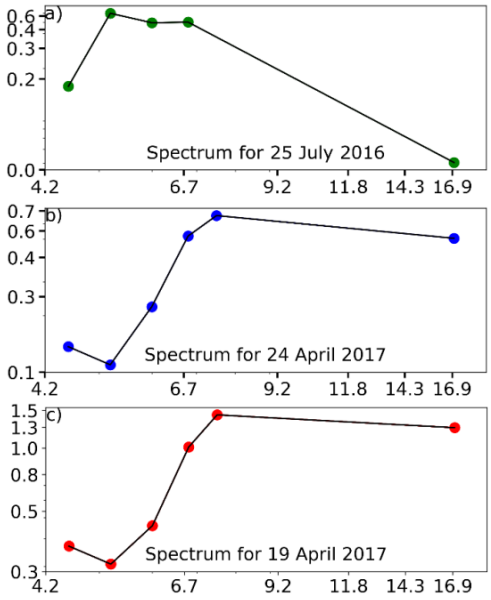

Figure 8. Spectra for 03:00 UT on July 25, 2016 (*a*); for 03:10 UT on April 24, 2017 (*b*); for 02:00 UT on April 19, 2017 (*c*). Colored circles indicate values of the total solar emission for each event. Along the X-axis are frequencies in GHz; along the Y-axis, fluxes in sfu

emission fluxes within the frames presented in Figure 7. Figure 8, *a* shows a spectrum obtained from SRH and NoRH data.

The spectrum is seen to be typical for the microwave emission generated by nonthermal electrons (gyrosynchrotron mechanism).

The source emission flux density level is lower than 1 sfu, and the response to this event was not observed in other ranges of electromagnetic emission.

The second structure is the filament observed on April 24, 2017 (Figure 9) at three SRH frequencies (4.5, 5.2, 6.0 GHz) during its rise and transformation into CME. The Figure also presents images obtained by NoRH at 17 GHz and by SDO at 304 Å. On the Sun In Time website [http://suntoday.lmsal.com/suntoday], the CME was recorded from 03:48 to 08:48 UT. The integral spectrum of the filament is shown in Figure 8, *b*. In this case, the difference between fluxes at frequencies of 7.5 and 17 GHz is relatively small and we can expect the bremsstrahlung mechanism of generation of the microwave emission.

The next structure with CME was found in the northwest of the solar limb on April 19, 2017 (Figure 10). There are images obtained at 4.5, 5.2, 6.0 GHz (SRH) and

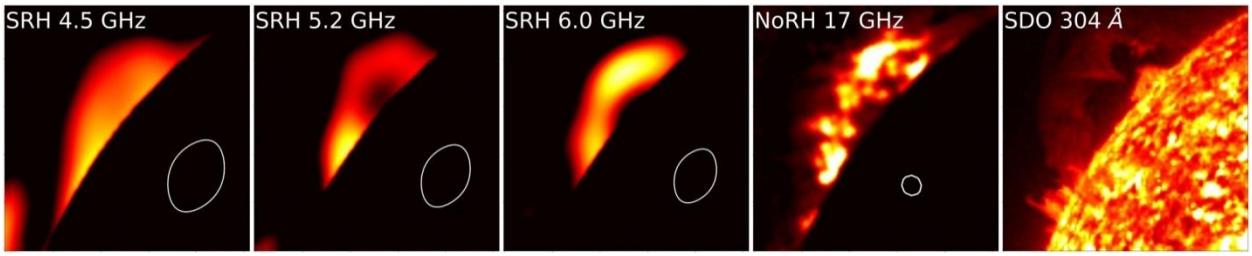

Figure 9. Rising filament at 03:10 UT on April 24, 2017. Images are constructed using data from (left to right): SRH at frequencies of 4.5, 5.2, and 6.0 GHz (white line marks the antenna pattern), NoRH at a frequency of 17 GHz, and SDO at a wavelength of 304 Å. Frame size is 400″×400″

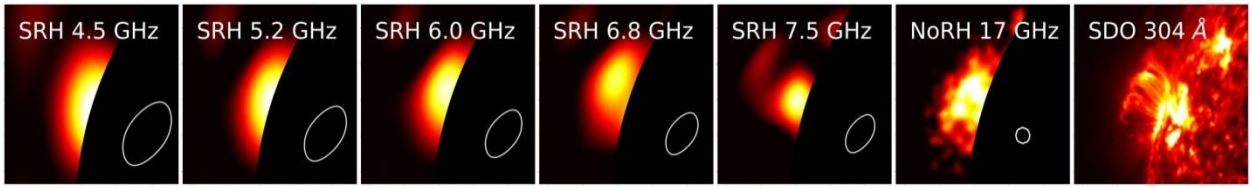

Figure 10. Local source in the north-west of the solar limb at 02:00 UT on April 19, 2017. Images are constructed using data from (left to right): SRH in a 4.5–7.5 GHz frequency range (white line marks the antenna pattern), NoRH at a frequency of 17 GHz, SDO at a wavelength of 304 Å. Frame size is 350″×350″

17 GHz (NoRH) at 02:00 UT. According to SDO data, the CME was visible at wavelengths of 171, 193, 211, 131, 335, 304, and 094 Å (in this case, the solar disk is not shaded in the rightmost image). The integral spectrum is similar to the spectrum for April 24 and matches the bremsstrahlung spectrum (see Figure 8, *c*).

Thus, in the case of the filament there are bremsstrahlung spectra, i.e. the flux intensity increases with frequency, and then remains constant. For a uniform source with thickness L, the frequency of transition to the flat spectrum corresponds to the transition of the emission mode to the optically thin one, i.e. when the dimensionless optical thickness $\tau \approx 1$. The value of τ depends on the emission frequency f, temperature T, and density n of emitting plasma:

$$\tau = 0.2 n^2 T^{-1.5} f^{-2} L. \quad (3)$$

The plasma temperature $T \approx T_b$ in the optically thick spectral region, i.e. when $f<7$ GHz. Unfortunately, the antenna beam width is larger than the filament angular size or comparable with it, which makes it impossible to measure T_b directly. We can estimate the brightness temperature from the flux F [sfu] and angular size of the source $\delta\Omega$ [arcsec^2] from Formula (4):

$$F = 7.2 \cdot 10^{11} T_b(f) f^2 \delta\Omega. \quad (4)$$

The angular size of the filaments (86×172 arcsec for April 24 at a frequency of 4.5 GHz and 78×195 arcsec for April 19 at a frequency of 4.5 GHz) can be estimated as $\delta\Omega \approx 1.5 \cdot 10^4$ arcsec^2, and the brightness temperature as $6 \cdot 10^3$ K and $1.5 \cdot 10^4$ K. We can now determine the emission measure $EM = n^2 L$ in these events by taking $\tau=1$ for $f=7.5$ GHz: $1.3 \cdot 10^{26}$ cm^{-5} and $5.2 \cdot 10^{26}$ cm^{-5}. The estimated emission measure is consistent with that derived in [Grechnev et al., 2008] for the plasma density (10^8–10^9 cm^{-3}) in the filament several tens of Mm thick.

CONCLUSION

The paper has presented a method for automatic calibration of SRH data in the 4–8 GHz frequency range, which allows us to eliminate contributions of local brightenings on the solar limb and above-the-limb sources. The method is suitable for calibration of relatively weak events, as well as for the quiet Sun. To calibrate bright sources requires cleaning images from side lobes.

An important feature of the method is the application of an artificial shading solar disk when constructing SRH images. Such a method of visualization of limb events will allow us to use SRH as a microwave coronagraph at several frequencies.

We have presented spectra for three events. The obtained values of the total solar emission are in agreement with those from the Nobeyama radioheliograph. We have also calculated sizes of objects along the line of sight.

The new approach enables us to confidently apply the method of automatic conversion of images, constructed using instrumental values of SRH radio brightness, into brightness temperatures to record events with low brightness by eliminating the nonuniform solar disk in the frequency range 4–8 GHz. The SRH light curves have demonstrated good agreement with the Nobeyama radioheliograph curves, indicating stability and fairly good quality of images enabling comparison based on time profiles. SRH is under modernization now and cannot resolve weak events with high spatial resolution yet.

The work was performed with budgetary funding of Basic Research program II.16.3.2. “Nonstationary and wave processes in the solar atmosphere”, the project “Primary energy release and turbulence in solar flares” under RAS Presidium Basic Research program KP 19-270 “Space: research into fundamental processes and their relationships”, as well as with the support of the Russian Science Foundation (Project No. 18-12-00172).

The experimental data were obtained using the Unique Research Facility Siberian Solar Radio Telescope [http://ckp-rf.ru/usu/73606]. Section 1.2 is based on data obtained using the equipment of Center for Common Use “Angara” [http://ckp-rf.ru/ckp/3056].

REFERENCES

Borovik V.N. Quiet Sun from multi frequency radio observations on RATAN-600. *Adv. Solar Phys*. 1994, vol. 43 pp. 185–190. DOI: 10.1007/3-540-58041-7_217.

Grechnev V.V., Lesovoi S.V., Smolkov G.Ya., et al. The Siberian solar radio telescope: the current state of the instrument, observations, and data. *Solar Phys*. 2003, vol. 216, iss. 1, pp. 239–272.

Grechnev V.V., Uralov A.M., Slemzin V.A., Chertok I.M., Kuzmenko I.V., Shibasaki K. Absorption phenomena and a probable blast wave in the 13 July 2004 eruptive event. *Solar Phys*. 2008, pp. 253–263. DOI: 10.1007/s11207-008-9178-8.

Kochanov A.A., Anfinogentov S. A., Prosovetsky D.V., Rudenko G.V., Grechnev V.V. Imaging of the solar atmosphere by the Siberian Solar Radio Telescope at 5.7 GHz with an enhanced dynamic range. *Publ. Astron. Soc. Japan*. 2013, vol. 65, iss. 19, pp. 1–12.

Lesovoi S., Kobets V. Correlation plots of the Siberian Radioheliograph. *Solar-Terr. Phys.* 2017, vol. 3, iss. 1, pp. 19–25. DOI: 10.12737/article_58f96eeb8fa318.06122835.

Lesovoi S.V., Altyntsev A.T., Kochanov A.A., Grechnev V.V., Gubin A.V., Zhdanov D.A., Ivanov E.F., Uralov A.M., Kashapova L.K., Kuznetsov A.A., Meshalkina N.S., Sych R.A. Siberian Radioheliograph: First results. *Solar-Terr. Phys.* 2017, vol. 3, iss. 1, pp. 3–18. DOI: 10.12737/article_58f96ec60fec 52.86165286

Nakajima H., Nishio M., Enome S., Shibasaki K., Takano T., Hanaoka Y., Torii C., Sekiguchi H., Bushimata T., et al. New Nobeyama radioheliograph. *Astrophys. J*. 1995, vol. 16, Suppl. iss., pp. 437–442.

Zirin H., Baumert B.M., Hurford G.J. The microwave brightness temperature spectrum of the quiet Sun. *Astrophys. J*. 1991, vol. 370, iss. 1, pp. 779–783.

URL: http://ru.iszf.irk.ru (accessed 20 June 2019).

URL: https://solar.nro.nao.ac.jp/norh/html (accessed 20 June 19).

URL: badary.iszf.irk.ru (accessed 20 June 2019).

URL: https://git.iszf.irk.ru/kochanov/srh48−api (accessed 20 June 2019).

URL: http://suntoday.lmsal.com/suntoday (accessed 20 June 2019).

URL: http://ckp-rf.ru/usu/73606 (accessed 20 June 2019).

URL: http://ckp-rf.ru/ckp/3056 (accessed 20 June 2019).

How to cite this article

Fedotova A.Yu., Altyntsev A.T., Kochanov A.A., Lesovoi S.V., Meshalkina N.S. Calibration of Siberian Radioheliograph images. *Solar-Terrestrial Physics*. 2019. Vol. 5. Iss. 4. P. 27–33. DOI: 10.12737/stp-54201904.